The Structure and Dynamics of Luminous and Dark Matter in the Early-Type Lens Galaxy of 0047-281 at z = 0.485

Koopmans, Léon V.E.; Treu, Tommaso

Published in:
The Astrophysical Journal

DOI:
10.1086/345423

The Astrophysical Journal, 583:606–615, 2003 February 1

THE STRUCTURE AND DYNAMICS OF LUMINOUS AND DARK MATTER IN THE EARLY-TYPE LENS GALAXY OF 0047−281 AT $z = 0.485$[1]

Léon V. E. Koopmans
TAPIR, California Institute of Technology, MS 130-33, Pasadena, CA 91125; leon@tapir.caltech.edu

and

Tommaso Treu
Department of Astronomy, California Institute of Technology, MS 105-24, Pasadena, CA 91125; tt@astro.caltech.edu
Received 2002 May 16; accepted 2002 October 7

ABSTRACT

We have measured the kinematic profile of the early-type (E/S0) lens galaxy in the system 0047−281 ($z = 0.485$) with the Echelle Spectrograph and Imager (ESI) on the W. M. Keck II Telescope, as part of the Lenses Structure and Dynamics (LSD) Survey. The central velocity dispersion is $\sigma = 229 \pm 15$ km s^{-1}, and the dispersion profile is nearly flat to beyond one effective radius (R_e). No significant streaming motion is found. Surface photometry of the lens galaxy is measured from *Hubble Space Telescope* images. From the offset from the local fundamental plane (FP), we measure an evolution of the effective mass-to-light ratio (M/L) of $\Delta \log(M/L_B) = -0.37 \pm 0.06$ between $z = 0$ and 0.485, consistent with the observed evolution of field E/S0 galaxies. (We assume $h_{65} = 1$, $\Omega_m = 0.3$, and $\Omega_\Lambda = 0.7$ throughout.) Gravitational lens models provide a mass of $M_E = (4.06 \pm 0.20) \times 10^{11}\ h_{65}^{-1}\ M_\odot$ inside the Einstein radius of $R_E = (8.70 \pm 0.07)\ h_{65}^{-1}$ kpc. This allows us to break the degeneracy between velocity anisotropy and density profile typical of dynamical models for E/S0 galaxies. We find that constant-M/L models, even with strongly tangential anisotropy of the stellar velocity ellipsoid, are excluded at more than 99.9% CL. The total mass distribution inside R_E can be described by a single power-law density profile, $\rho_t \propto r^{-\gamma'}$, with an effective slope $\gamma' = 1.90^{+0.05}_{-0.23}$ (68% CL; ±0.1 systematic error). Two-component models yield an upper limit (68% CL) of $\gamma \leq 1.55(1.12)$ on the power-law slope of the dark matter density profile and a projected dark matter mass fraction of $0.41(0.54)^{+0.15}_{-0.05}{}^{(+0.09)}_{(-0.06)}$ (68% CL) inside R_E, for Osipkov-Merritt models with anisotropy radius $r_i = \infty(R_e)$. The stellar M_*/L values derived from the FP agree well with the maximum allowed value from the isotropic dynamical models (i.e., the "maximum-bulge solution"). The fact that both lens systems 0047−281 ($z = 0.485$) and MG 2016+112 ($z = 1.004$) are well described inside their Einstein radii by a constant-M_*/L stellar mass distribution embedded in a nearly logarithmic potential—with an isotropic or a mildly radially anisotropic dispersion tensor—could indicate that E/S0 galaxies underwent little *structural evolution* at $z \lesssim 1$ and have a close-to-isothermal total mass distribution in their inner regions. Whether this conclusion can be generalized, however, requires the analysis of more systems. We briefly discuss our results in the context of E/S0 galaxy formation and cold dark matter simulations.

Subject headings: galaxies: elliptical and lenticular, cD — galaxies: evolution — galaxies: formation — galaxies: kinematics and dynamics — galaxies: structure — gravitational lensing

1. INTRODUCTION

To understand the evolution and internal structure of luminous and dark matter in early-type galaxies (E/S0), we have started the Lenses Structure and Dynamics (LSD) Survey. From an observational point of view, the LSD Survey aims at measuring—using the Keck II Telescope—the internal (stellar) kinematics of a relatively large sample of E/S0 gravitational lens galaxies in the redshift range $z = 0$–1 (see Treu & Koopmans 2002, hereafter TK02, for a description of the survey and its scientific rationale). The stellar kinematic profiles are combined with constraints from a gravitational lensing analysis—in particular the mass enclosed within the Einstein radius—in order to break degeneracies inherent to each method individually. In this way, we are uniquely able to constrain the luminous and dark mass distribution and the velocity ellipsoid of the luminous (i.e., stellar) component.

Several of the main questions about E/S0 galaxies that we aim to answer with the LSD Survey are (1) What is the amount of dark matter within the inner few effective radii (R_e)? (2) Does the dark matter density profile agree with the universal profiles inferred from cold dark matter (CDM) simulations (Navarro, Frenk, & White 1997, hereafter NFW; Moore et al. 1998; Ghigna et al. 2000)? (3) Is there a universal total (luminous plus dark matter) density distribution that well describes the inner regions of E/S0 galaxies? If so, is it isothermal, as observed in the local universe and often assumed in lensing analyses? (4) How does the stellar mass-to-light ratio (M/L) of E/S0 galaxies evolve with redshift, and does it agree with the evolution of the stellar populations of field early-type galaxies as inferred from fundamental plane (FP) measurements (Treu et al. 1999, 2001a, 2002, hereafter T99, T01a, T02, respectively; Kochanek et al. 2000; van Dokkum et al. 2001)? (5) Does the struc-

[1] Based on observations collected at W. M. Keck Observatory, which is operated jointly by the California Institute of Technology and the University of California, and with the NASA/ESA *Hubble Space Telescope*, obtained at STScI, which is operated by the Association of Universities for Research in Astronomy (AURA), Inc., under NASA contract NAS 5-26555.

ture of E/S0 galaxies evolve between $z = 0$ and 1, or is the evolution of the FP purely an evolution of the stellar population? (6) Is the stellar velocity dispersion tensor isotropic or anisotropic?

First results from the LSD Survey were presented in two recent papers (Koopmans & Treu 2002, hereafter KT02; TK02), where we combined our measurement of the luminosity-weighted stellar velocity dispersion of the lens galaxy in MG 2016+112 at $z = 1.004$ with the mass enclosed by the Einstein radius as determined from gravitational lens models (Koopmans et al. 2002). A robust constraint was found on the slope of the total density profile of the lens galaxy, i.e., $\gamma' = 2.0 \pm 0.1 \pm 0.1$ (random and systematic errors) for $\rho_t \propto r^{-\gamma'}$. In addition, we were able to determine the stellar mass-to-light ratio and constrain the slope of the dark matter halo, leading to a relatively simple self-consistent picture of the lens galaxy: an old and metal-rich stellar component embedded in a logarithmic (i.e., isothermal) potential observed at a look-back time of $\sim$8 Gyr—remarkably similar to many present-day E/S0 galaxies. Constant-M/L models were ruled out at a very high confidence level, and a significant mass fraction ($\sim$75%) of dark matter was shown to be present inside the Einstein radius of about 13.7 kpc. Unfortunately, given the faintness of the galaxy at $z = 1$, only a luminosity-weighted velocity dispersion could be obtained and only minimal constraints could be set on the anisotropy of stellar orbits.

In this paper, we present Keck and *Hubble Space Telescope* (*HST*) observations, a gravitational lens model, and a dynamical model of the lens galaxy in 0047−281 at $z = 0.485$ (Warren et al. 1996, 1998, 1999). This galaxy is bright and sufficiently extended that we were able to measure a spatially resolved velocity dispersion profile, thus setting unprecedented constraints on the orbital structure of a galaxy at a look-back time of $\sim$5 Gyr.

The paper is organized as follows. In § 2, we describe archival *HST* observations and spectroscopic observations with the Echelle Spectrograph and Imager (ESI) on the Keck II Telescope. In § 3, we analyze these observations and determine the luminosity evolution of the lens galaxy with respect to the local FP. In § 4, we present a gravitational lens model, from which we determine the mass enclosed by the Einstein radius. In § 5, we present a model for the luminous and dark matter distributions of the lens galaxy. In § 6, the results from the dynamical models are presented. Section 7 summarizes and discusses the results.

In the following, we assume that the Hubble constant, the matter density, and the cosmological constant are $H_0 = 65\ h_{65}$ km s^{-1} Mpc^{-1}, $\Omega_m = 0.3$, and $\Omega_\Lambda = 0.7$, respectively. Throughout this paper, r is the radial coordinate in three-dimensional space, while R is the radial coordinate in two-dimensional projected space.

2. OBSERVATIONS

2.1. *HST Imaging*

Wide Field and Planetary Camera 2 (WFPC2) images of the system are available from the *HST* archive, through filters F555W and F814W.[2] In particular, the system has been imaged for 9500 s in F555W on the Wide-Field Camera, and 2700 s in F814W on the Planetary Camera.

The images were reduced using a series of IRAF scripts based on the IRAF package DRIZZLE (Fruchter & Hook 2002), to align the independent pointings and perform cosmic-ray rejection. A subsampled (pixel scale 0.″05) image was produced for the F555W image. The final "drizzled" image in F555W is shown in Figure 1. Note that for the redshift of the source, $z = 3.595$, Lyα is redshifted to 5589 Å (Warren et al. 1998) and that the F555W magnitude therefore includes the bright Lyα emission. The F814W image is significantly shallower than the F555W image, and although adequate for measuring the structural parameters,

[2] Obtained as part of the CASTLES Survey.

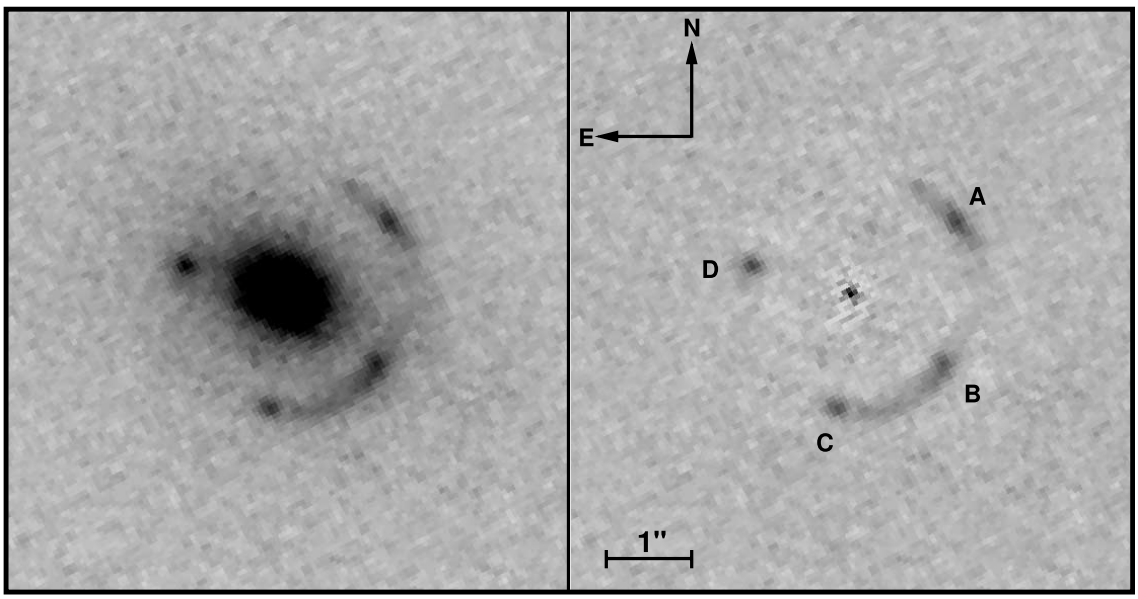

FIG. 1.—*Left*: *HST* F555W image of 0047−281. The images designated A–D run clockwise from the upper right, as shown in right-hand panel. *Right*: Same image with a smooth galaxy model subtracted. Note the almost continuous ring structure including images A, B, and C.

TABLE 1
OBSERVED SPECTROPHOTOMETRIC QUANTITIES OF THE LENS GALAXY G IN 0047−281

Parameter	Value
Redshift (G)	0.485 ± 0.001
F814W	18.67 ± 0.09 mag
F555W	20.61 ± 0.09 mag
$SB_{e,F814W}$	20.23 ± 0.22 mag arcsec^{-2}
$SB_{e,F555W}$	22.59 ± 0.07 mag arcsec^{-2}
$R_{e,F814W}$	$0\farcs82 \pm 0\farcs12$
$R_{e,F555W}$	$0\farcs99 \pm 0\farcs04$
b/a (1−e)	0.80 ± 0.10
Major-axis P.A.	$67^\circ \pm 5^\circ$
Rest-Frame Quantities	
σ	229 ± 15 km s^{-1}
$M_V - 5\log h_{65}$	-22.90 ± 0.04 mag
$M_B - 5\log h_{65}$	-22.22 ± 0.11 mag
$R_{e,V}$	$5.21 \pm 0.72\, h_{65}^{-1}$ kpc
$R_{e,B}$	$5.82 \pm 0.58\, h_{65}^{-1}$ kpc
$SB_{e,V}$	19.29 ± 0.22 mag arcsec^{-2}
$SB_{e,B}$	20.39 ± 0.11 mag arcsec^{-2}

NOTES.—The second part of the table lists rest-frame quantities, derived from the observed quantities as described in § 2. Note that σ is the central velocity dispersion corrected to a circular aperture of radius $R_e/8$. All quantities in this table assume $H_0 = 65$ km s^{-1} Mpc^{-1}, $\Omega_m = 0.3$, and $\Omega_\Lambda = 0.7$.

it is not particularly useful for the lens modeling, since the multiple images are faint and their positions cannot be accurately determined.

Surface photometry was performed on the F555W and F814W images as described in T99 and Treu et al. (2001b, hereafter T01b). The galaxy brightness profiles are well represented by an $R^{1/4}$ profile, which we fit—taking the *HST* point-spread function into account—to obtain the effective radius (R_e), the effective surface brightness (SB_e), and the total magnitude. The relevant observational quantities of galaxy G in 0047−281 and their errors are listed in Table 1. Note that errors on SB_e and R_e are tightly correlated and that the uncertainty on the combination $\log R_e - 0.32SB_e$ that enters the FP (see § 3) is very small (∼0.015; see Kelson et al. 2000; T01b; Bertin, Ciotti, & del Principe 2002). In the right-hand panel of Figure 1, we show the *HST* image after removal of a smooth model for the lens galaxy. Notice the nearly circular structure of the lensed image configuration around the lens galaxy.

Rest-frame photometric quantities listed in Table 1—computed as described in T01b—are corrected for Galactic extinction using $E(B-V) = 0.016$ from Schlegel, Finkbeiner, & Davis (1998).

2.2. *Keck Spectroscopy*

We observed 0047−281 using the Echelle Spectrograph and Imager (ESI; Sheinis et al. 2002) on the Keck II Telescope during four consecutive nights (2001 July 23–26), for a total integration time of 20,700 s (7×1800 s + 3×2700 s). The seeing was good ($0\farcs6 <$ FWHM $< 0\farcs8$), and three of four nights were photometric. Between exposures, we dithered along the slit to allow for a better removal of sky residuals in the red end of the spectrum. The slit (20″ in length) was aligned with the major axis of the galaxy. The slit width of 1.″25 yields an instrumental resolution of 30 km s^{-1}, which is adequate for measuring the stellar velocity dispersion and removing narrow sky emission lines. The centering of the galaxy in the slit was constantly monitored by means of the ESI viewing camera (the galaxy was bright enough to be visible in a few seconds exposure), and we estimate the centering perpendicular to the slit to be accurate to $\lesssim 0\farcs1$.

TABLE 2
KINEMATIC DATA ALONG THE MAJOR AXIS OF 0047−281

Aperture (arcsec^2)	σ (km s^{-1})	$\Delta\sigma$ (km s^{-1})
(0.0–0.2) × 1.25	219	12
(0.2–0.8) × 1.25	212	14
(0.8–1.4) × 1.25	205	13

NOTE.—The adjacent rectangular apertures are indicated. The seeing was 0.″7 during the observations.

Data reduction was performed using the IRAF package EASI2D,[3] as described in KT02. To preserve most of the spatially resolved information and to achieve an adequate signal-to-noise ratio at the largest distance for the center of the galaxy, we defined five apertures along the spatial direction of the spectrum and summed the signal within each aperture. The apertures correspond approximately to angular dimensions along the slit $0\farcs6 \times 1\farcs25$, $0\farcs6 \times 1\farcs25$, $0\farcs4 \times 1\farcs25$, $0\farcs6 \times 1\farcs25$, and $0\farcs6 \times 1\farcs25$ (centered at $-1\farcs1$, $-0\farcs5$, $0''$, $0\farcs5$, and $1\farcs1$, respectively, along the major axis). A velocity dispersion profile was measured with the Gauss-Hermite pixel-fitting software (van der Marel 1994) and the Gauss-Hermite Fourier-fitting software (van der Marel & Franx 1993) on the spectral region including the G band (∼4304 Å), using as kinematic templates spectra of G–K giants observed at twilight with a 0.″3 slit width, appropriately smoothed to match the instrumental resolution of the 1.″25 slit. The two codes provide consistent measurements. The total error on velocity dispersion was estimated by adding in quadrature the formal uncertainty given by the codes, the scatter in the results obtained with different templates, and the semidifference of the results obtained with the two codes. The fit to the spectrum from the aperture including part of the brightest lensed images (A and B in Fig. 1) was poor, with severe mismatch and unstable measurements. We interpret this as due to contamination by emission from the lensed images. We discarded this measurement from the analysis. The velocity dispersion profile was then folded around the center, as determined by fitting the centroid of the light distribution at the wavelength of the G band, and the velocity dispersion averaged in the corresponding apertures (symmetric apertures provided results within the errors). The final results are listed in Table 2.

Using the procedure detailed in T01b, the value in the central aperture can be corrected to a standard central velocity dispersion of $\sigma = 229 \pm 15$ km s^{-1} within a circular aperture of radius $R_e/8$ (see also § 6.1). No evidence for significant streaming motions (e.g., rotation) was found, with an upper limit of 50 km s^{-1} relative radial velocity between the center and the outermost aperture.

[3] Developed by D. Sand and T. Treu (D. Sand et al. 2003, in preparation).

3. THE FUNDAMENTAL PLANE AND THE EVOLUTION OF STELLAR POPULATIONS

Early-type galaxies in the local universe occupy approximately a plane in the three-dimensional space defined by the parameters effective radius ($\log R_e$), effective surface brightness (SB_e), and central velocity dispersion ($\log \sigma$)

$$\log R_e = \alpha \log \sigma + \beta SB_e + \gamma_{FP} \quad (1)$$

and known as the fundamental plane (FP; Dressler et al. 1987; Djorgovski & Davis 1987).

In recent years, it has been shown that a similar correlation between those observables exists in clusters out to $z \sim 0.8$ (see, e.g., van Dokkum & Franx 1996; Kelson et al. 1997; Bender et al. 1998; Pahre 1998; van Dokkum et al. 1998; Jørgensen et al. 1999; Ziegler et al. 2001). The observed evolution of the intercept γ_{FP} of the FP with redshift is consistent with the expectations of passive evolution models for an old stellar population (redshift of formation $z_f \gtrsim 2$; see, e.g., van Dokkum et al. 1998). No evidence for a dramatic evolution of the slopes α and β of the FP with redshift is found with the available data (see Jørgensen et al. 1999, Kelson et al. 2000, and T01a for discussion). The correlation is also observed to be tight in intermediate-redshift field samples, although a faster evolution of the intercept is found in the highest-redshift field samples (to $z \sim 0.7$), and interpreted as evidence for secondary episodes of star formation in the field population at $z < 1$ (T02; see also T99; T01a; Kochanek et al. 2000; van Dokkum et al. 2001; Trager et al. 2000).

Assuming that galaxy G in 0047−281 lies on an FP with slopes similar to those in the local universe—and pure luminosity evolution—we can determine the offset of its effective mass-to-light ratio ($M/L \propto \sigma^2 10^{-0.4 SB_e}/R_e$) with respect to the local relation, which is related to the evolution of the intercept by $\Delta \log(M/L) = -0.4 \Delta\gamma_{FP}/\beta$. As the local FP in the B band we adopt the relation found by Bender et al. (1998), i.e., $\alpha = 1.25$, $\beta = 0.32$, and $\gamma_{FP} = -8.895 - \log h_{50}$. In this way, we obtain $\Delta \log(M/L_B) = -0.37 \pm 0.06$. The error is dominated by the observed FP parameters of galaxy G and dominates uncertainties on the local FP relation. In Figure 2, we plot the evolution of the effective M/L for cluster and field E/S0 galaxies as function of redshift (*dashed and solid lines, respectively*; from T02), together with the value obtained for galaxy G (*square at* $z = 0.485$). The effective M/L evolution for galaxy G is consistent with what is observed for field galaxies, i.e., faster than for the cluster sample, possibly indicating younger luminosity-weighted stellar populations (see, e.g., T01a, T02). As described and discussed in TK02, we can use this measurement to infer the stellar M/L (M_*/L_B) of galaxy G, assuming that

$$\log(M_*/L_B)_z = \log(M_*/L_B)_0 + \Delta \log(M/L_B) \ , \quad (2)$$

where the second term on the right-hand side of the equation is measured from the evolution of the FP and the first term on the right-hand side of the equation can be measured for local E/S0 galaxies. Note that equation (2) uses the nontrivial assumption that the stellar mass is a redshift-independent function of the combination of observables used to define the effective mass $\sigma^2 R_e$ (for a full discussion, see T02 and TK02). Using the local value of $(7.3 \pm 2.1)\ h_{65}\ M_\odot / L_{B,\odot}$ determined from data by Gerhard et al. (2001) as in TK02, we infer $M_*/L_B = (3.1 \pm 1.0)\ h_{65}\ M_\odot/L_{B,\odot}$ for galaxy G.

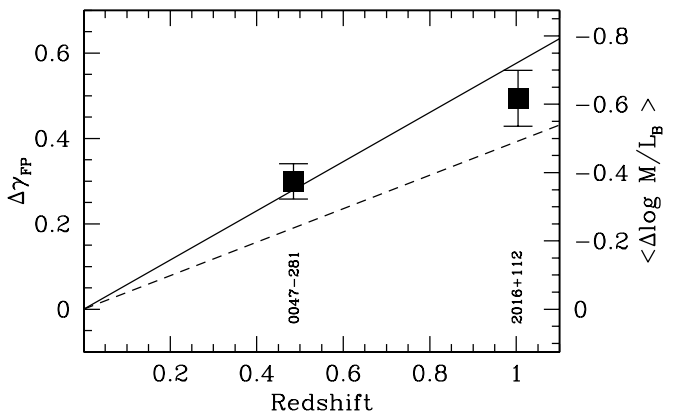

FIG. 2.—Evolution of the M/L as inferred from the evolution of the FP. Solid and dashed lines indicate linear fits to the M/L evolution for field (T02) and cluster E/S0 galaxies (van Dokkum et al. 2001), respectively. The square at $z = 1.004$ indicates the M/L evolution of galaxy D in MG 2016+112 (KT02), while the square at $z = 0.485$ represents galaxy G in 0047−281.

4. GRAVITATIONAL LENS MODEL

The Einstein radius (R_E) and mass enclosed by the Einstein radius, i.e., $M_E \equiv M(< R_E)$, are quantities required in the dynamical models that are discussed in § 5. Both R_E and M_E are very insensitive to the assumed mass profile (see, e.g., Kochanek 1991), especially for highly symmetric cases like 0047−281 (see Fig. 1). For consistency—to ensure uniform modeling throughout the LSD Survey—we model the lens galaxy (Fig. 3) as a singular isothermal ellipsoid (SIE;

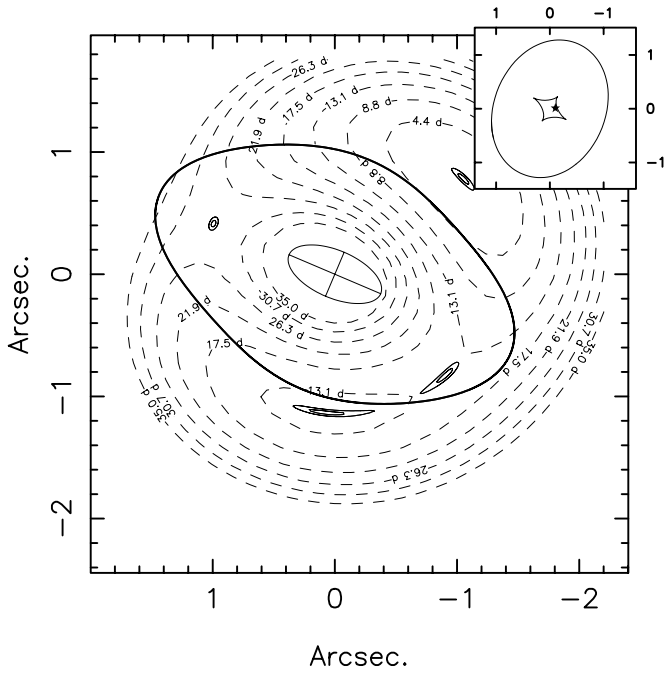

FIG. 3.—Simple gravitational lens model of 0047−281. The crosshaired ellipse indicates the position, position angle, and ellipticity of the lens galaxy. The thick solid contour is the critical curve, whereas the dashed contours indicate the time delay surface. To guide the eye, the lensed images are indicated by two solid contours corresponding to circles in the source plane with 15 and 30 mas radius. The inset shows a zoom-in of the caustics. The source position is indicated by a star.

Kormann, Schneider, & Bartelmann 1994; see also Chen, Kochanek, & Hewitt 1995; Kochanek 1995; Grogin & Narayan 1996; Koopmans & Fassnacht 1999; Cohn et al. 2001; Muñoz, Kochanek, & Keeton 2001; Rusin et al. 2002). Although the assumption of an SIE mass distribution might not be accurate enough for some applications (see, e.g., Saha 2000; Rusin & Tegmark 2001; Wucknitz 2002), we again stress that this choice of the mass profile does *not* significantly bias the determination of the quantities used in our analysis, i.e., $M_{\rm E}$ and $R_{\rm E}$. The reason is not only that the image deflection angles in four-image systems like 0047−281 are nearly the same, but also that the deflection angle is only a function of the enclosed mass and therefore is little affected by either the radial mass profile or the ellipticity of the lens (see § 3 in Kochanek 1991 for a more detailed discussion). Constraints on the mass density profile obtained in § 5 are therefore virtually *independent* of the choice of lens mass model.

The centroids of the four lensed images are used as constraints on the lens model (Table 3), assuming errors of 10 mas, i.e., a fifth of a drizzled pixel size. We do not use the flux ratios in our analysis, since they are not only difficult to measure accurately for extended images, but also change as function of position along the arcs and could be affected by differential dust extinction (see, e.g., Surpi & Blandford 2003). The position and position angle of the lens galaxy mass distribution are set equal to those of its surface brightness distribution (Table 1), and the presence of an external shear is allowed for. Hence, there are six free parameters (i.e., the ellipticity and velocity dispersion of the lens galaxy mass distribution, the source position, and the external shear), eight constraints (i.e., the four image positions), and consequently, 2 degrees of freedom (dof). The velocity dispersion of the SIE mass model is defined so that the mass enclosed by the critical curve is equal to that inside the Einstein radius of a singular isothermal sphere with the same velocity dispersion (Kormann et al. 1994).

The best solution for a single SIE mass distribution yields $\sigma_{\rm SIE} = 253$ km s^{-1} for the lens galaxy, whereas the required external shear is 0.13. The χ^2 is rather high, 306 for 2 dof. It is possible to devise more elaborate models (for example, with a dwarf companion) that fit the observational constraints much better. However, as mentioned above, the mass enclosed by the Einstein radius is very insensitive to the precise lensing model. As an illustration of the uncertainty related to the mass modeling, we considered including a dwarf companion galaxy with $\sigma_{\rm SIE} \sim 60$ km s^{-1}. Although the fit is greatly improved ($\chi^2 = 0$, because there are more free parameters than constraints), the velocity dispersion of the primary lens changes by only -4 km s^{-1}. We therefore do not elaborate further on the details of the lens model—which is not the intention of this paper—and we use the results from SIE mass model in the rest of the analysis. More detailed lens models are being constructed based on the structure in the lensed arcs (R. Webster 2002, private communication).

TABLE 3
Centroid Image Positions of 0047−281 with Respect to the Centroid of the Primary Lens Galaxy G

Image	Δx (arcsec)	Δy (arcsec)	$\delta(x, y)$ (mas)
G	≡0.000	≡0.000	...
A	+1.048	+0.726	10, 10
B	+0.896	−0.802	10, 10
C	−0.126	−1.165	10, 10
D	−1.011	+0.263	10, 10

We note that $\sigma_{\rm SIE}$ is close to the central stellar velocity dispersion (Table 1). However, we emphasize that $\sigma_{\rm SIE}$ is a model-dependent expression of the well-determined total enclosed mass, while the central stellar velocity dispersion depends on the precise total mass profile, on the luminous mass profile, and on the dynamical state of the luminous component. Hence, the two quantities do not have to agree in principle. Their agreement is rather an indication of a regular behavior in the physical properties of early-type galaxies, as discussed in §§ 5, 6, and 7 (see also Kochanek 1994 and Kochanek et al. 2000).

The adopted SIE velocity dispersion corresponds to a circular Einstein radius of $R_{\rm E} = (8.70 \pm 0.07)\, h_{65}^{-1}$ kpc (i.e., $\theta_{\rm E} = 1\farcs34 \pm 0\farcs01$) and an enclosed mass of $M_{\rm E} = 4.06 \times 10^{11}\, h_{65}^{-1}\, M_\odot$. The errors on $R_{\rm E}$ and $M_{\rm E}$ are correlated (both depend on $\sigma_{\rm SIE}$): for fixed $R_{\rm E}$ one finds that $\delta M_{\rm E}/M_{\rm E} = 2(\delta\sigma_{\rm SIE}/\sigma_{\rm SIE})$. This error corresponds to about 3% for $\delta\sigma = 4$ km s^{-1}, i.e., the difference between the model with and without an additional companion galaxy, which we adopt as systematic error (the random error on $\sigma_{\rm SIE}$ is a negligible 0.5%). If a wide range of mass profiles and/or ellipticities are adopted, the enclosed mass changes by $\lesssim$4% for symmetric four-image systems like 0047−281 (see, e.g., Kochanek 1991). Hence, adding the two contributions in quadrature, we find a total error of 5% on $M_{\rm E}$ inside a radius of $R_{\rm E} \equiv 8.70\, h_{65}^{-1}$ kpc.

5. DYNAMICAL MODEL

Following TK02, we model the galaxy mass distribution as a superposition of two spherical components, one for the luminous stellar matter and one for the dark matter halo.[4] The luminous mass distribution is described by a Hernquist (1990) model,

$$\rho_L(r) = \frac{M_* r_*}{2\pi r (r + r_*)^3}\ , \tag{3}$$

where M_* is the total stellar mass. This profile well reproduces the $R^{1/4}$ surface brightness profile for $r_* = R_e/1.8153$. In § 6.1, we also examine the effect of a steeper inner core, $\rho_L(r) \propto r^{-2}$, using the Jaffe (1983) model. We find the effect to be negligible within the errors. The dark matter distribution is modeled as

$$\rho_d(r) = \frac{\rho_{d,0}}{(r/r_b)^\gamma \left[1 + (r/r_b)^2\right]^{(3-\gamma)/2}}\ , \tag{4}$$

which closely describes an NFW profile for $\gamma = 1$ and has the typical asymptotic behavior at large radii ($\propto r^{-3}$) found from numerical simulations of dark matter halos (see, e.g., Ghigna et al. 2000). See TK02 for further discussion of this mass profile and dynamical model.

[4] Spherical dynamical models provide an adequate approximate description for computing kinematic quantities of E/S0 galaxies with axis ratio $b/a \sim 0.8$, like 0047−281 (see, e.g., Saglia, Bertin, & Stiavelli 1992; Kronawitter et al. 2000), even though clearly they are not appropriate for the lensing analysis, since, e.g., they do not produce quadruply lensed images.

According to the CDM simulations given in Bullock et al. (2001), a galaxy with the virial mass of galaxy G at $z = 0.485$ has $r_b \approx 50$ kpc $\gg R_e \sim R_{\rm E}$. Hence, in the light of a comparison with CDM models, we can safely assume that the dark matter profile in the region of interest (i.e., inside $\sim R_{\rm E}$) is well described by a power law $\rho_d \propto r^{-\gamma}$. Throughout this study, we set $r_b = 50$ kpc (effectively equal to $r_b = \infty$). The effects of changing r_b are discussed in TK02.

In addition, we assume an Osipkov-Merritt (Osipkov 1979; Merritt 1985a, 1985b) parameterization of the anisotropy β of the luminous mass distribution,

$$\beta(r) = 1 - \frac{\sigma_\theta^2}{\sigma_r^2} = \frac{r^2}{r^2 + r_i^2} \ , \qquad (5)$$

where σ_θ and σ_r are the tangential and radial components, respectively, of the velocity dispersion and r_i is called the anisotropy radius. Note that $\beta > 0$ by definition, not allowing tangentially anisotropic models. A brief discussion of tangentially anisotropic models with negative constant values of β is given in § 6.2. As a further caveat, note that at infinite radii, Osipkov-Merritt models become completely radial. Although this behavior is not commonly found within the inner regions of E/S0 galaxies probed by observations (see, e.g., Gerhard et al. 2001; but see van Albada 1982 and Bertin & Stiavelli 1993 for theoretical grounds), it has little effect in the case considered here, since the pressure tensor only becomes significantly radial well outside the Einstein radius and in projection is significantly downweighted by the rapidly falling luminosity-density profile.

The line-of-sight velocity dispersion is obtained by solving the three-dimensional spherical Jeans equation (see, e.g., eq. [4-30] in Binney & Tremaine 1987) for the luminous component in the total gravitational potential and computing the luminosity-weighted average along the line of sight (eq. [4-60] in Binney & Tremaine 1987; see also, e.g., Ciotti, Lanzoni, & Renzini 1996). We correct for the average seeing of 0.″7 during the observations and average the velocity dispersion—weighted by the surface brightness—inside the appropriate rectangular apertures. For completeness, we rescale the apertures (see Table 2) by 0.9 and 1.1 in the directions of the major and minor axes, respectively, so that their projection on the axisymmetric model is equivalent to their projection on an elliptical galaxy with an axial ratio of 0.8, even though this has minimal effects on the model velocity dispersions (<1%), much smaller than the observational errors. The uncertainties on seeing, aperture size, and galaxy centering are taken into account as systematic errors in the following discussion.

6. LUMINOUS AND DARK MATTER IN 0047−281

The unknown parameters of our dynamical model are M_*, γ, r_i, and $\rho_{d,0}$ (we note again that $r_* = R_e/1.8153$ and $r_b = 50$ kpc). We can eliminate one of these parameters using $M_{\rm E}$, the mass inside the Einstein radius, which is the most accurately known constraint on the lens mass model. We choose to eliminate $\rho_{d,0}$. In addition, we transform M_* into the stellar M/L, M_*/L_B, fixing the model luminosity exactly to the value $1.2 \times 10^{11}\ h_{65}^{-2}\ L_{B,\odot}$. Hence, values of M_*/L_B that we derive from the dynamical model bear an additional uncertainty of 11%, i.e., the observational error on L_B, whereas M_*, which is used in the model calculation, does not have this error. We use the average $R_e = (5.52 \pm 0.55)\ h_{65}^{-1}$ kpc of the rest-frame V- and B-band values.

For any given set $\{M_*/L_B, \gamma\}$, the dynamical model is completely determined and the luminosity-weighted velocity dispersions for each of the three apertures (see Table 2) can be computed. The likelihood is determined assuming Gaussian error distributions and the confidence contours using the likelihood ratio statistic.[5]

6.1. *Power-Law Models*

Before studying the luminous and dark matter profiles individually, we determine the effective slope (γ') of the total (luminous *plus* dark) matter density profile (ρ_t) inside the Einstein radius. We emphasize that an effective slope of γ' does not imply that the density profile follows $\rho_t \propto r^{-\gamma'}$ exactly, but only *effectively*.

For MG 2016+112 (TK02), we measured an effective slope $\gamma' = 2.0 \pm 0.1 \pm 0.1$ (random and systematic errors), assuming $\rho_t \propto r^{-\gamma'}$. Based on the data in Warren et al. (1998) and Kochanek et al. (2000), we found a similar effective slope for 0047−281. However, the errors were relatively large because of a lack of an extended kinematic profile and the large uncertainty on the velocity dispersion given by Warren et al. (1998). With the data presented here, we can perform a more accurate measurement and set constraints on the anisotropy of the velocity ellipsoid.

In Figure 4*c*, we show the likelihood contours of γ' versus the anisotropy radius r_i, based on our extended kinematic profile of 0047−281. Three main conclusions can be drawn: (1) for a spherical isotropic stellar distribution function ($r_i \to \infty$), $\gamma' = 1.90 \pm 0.05$ (68% CL) (see also Fig. 5); (2) a lower limit of $r_i/R_e \gtrsim 0.7$ (68% CL) can be set, implying that the velocity distribution function is isotropic in the inner regions of the galaxy; and (3) independent of r_i, one finds $\gamma' = 1.90^{+0.05}_{-0.23}$ (68% CL).

To assess systematic errors on γ', we varied $M_{\rm E}$ and R_e by the total uncertainties ±5% and ±10%, respectively. The value of γ' required to fit the data changes by ±0.05 and ±0.03, respectively. Other potential sources of errors, such as seeing, aperture corrections, and aperture offsets, were found to be negligible. We add both contributions, and we conservatively round up to a total systematic error of ±0.1, to account for all potential minor sources of error.

Although the outer region of galaxy G is well fitted by a Hernquist (1990) model, the inner region, with $\rho_L(r) \propto r^{-1}$, is less constrained because of the finite resolution of the *HST* images. We therefore examined power-law models with steeper inner luminosity density profiles, $\rho_L(r) \propto r^{-2}$, using the model from Jaffe (1983). For both $r_i = \infty$ and $r_i = R_e$, we find that the stellar velocity dispersions change by ≤ 6 km s^{-1}. In general, Jaffe models give slightly lower velocity dispersions for a fixed value of γ', and the best-fit models therefore yield slightly higher values of γ' (by a few hundredths) compared with the Hernquist models. However, the differences are not significant, given the errors on the dispersion profile, and therefore we conclude that our

[5] Note that the likelihood ratio statistic is distributed as a χ^2 only asymptotically; hence, the interpretation of the likelihood ratio contours as confidence contours is an approximation. However, because the confidence contours (i.e., Fig. 4) on which we base our results only mildly deviate from true ellipses—i.e., the limiting case for large numbers of constraints—this approximation should work well.

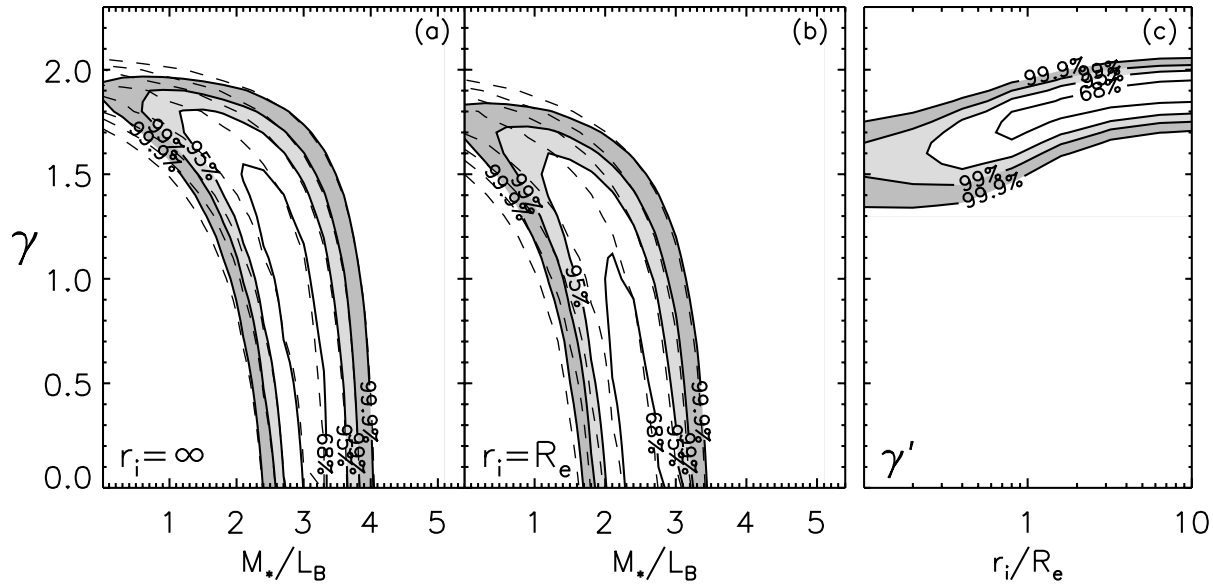

FIG. 4.—(*a*) and (*b*) Likelihood contours of the inner slope of the dark matter halo (γ) vs. the stellar M/L (M_*/L_B) for the lens galaxy in 0047−281, for $r_i = \infty$ and $r_i = R_e$, respectively. (The mass enclosed within the Einstein radius is fixed to $M_{\rm E}$; see § 6 for details.) Dashed lines indicate the likelihood contours from the dynamical model only, whereas the solid lines combine the constraints from the dynamical model and the FP. (*c*) Likelihood contours of the effective slope (γ') vs. the anisotropy radius (r_i). All models assume $r_b = 50$ kpc. See text for a more comprehensive description of the models.

results are insensitive to the precise shape of the inner luminosity density profile.

For completeness, we note that our model with $\gamma' = 1.90$ results in a central stellar velocity dispersion of $\sigma = 221$ km s^{-1} inside $R_e/8$, in excellent agreement with the empirically derived value of $\sigma = 229 \pm 15$ km s^{-1} in § 2.2, confirming the self-consistency of our models.

In conclusion, the total mass distribution of galaxy G is well matched by a single power-law density profile that is isothermal (i.e., $\rho_t \propto r^{-2}$) to within ∼5%, and the velocity ellipsoid of the luminous component is isotropic, at least inside ∼70% of the effective radius. Note that this limit is generally consistent with the limits set by other physical considerations. In fact, strongly radial orbits would result in radial instability (e.g., Merritt & Aguilar 1985 find that Osipkov-Merritt models with an initial Jaffe density profile are unstable for $r_i \lesssim 0.3 r_0$, where $r_0 \approx R_e/0.763$ is the Jaffe half-mass radius; for the effects of a dark matter halo, see, e.g., Stiavelli & Sparke 1991) or negative values of the distribution function (see, e.g., Ciotti 1999 and references therein).

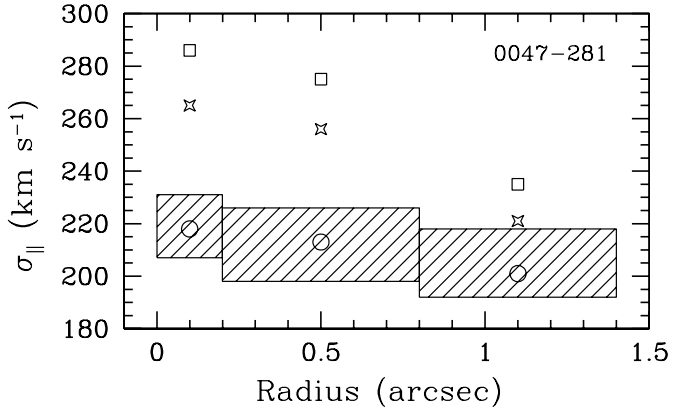

FIG. 5.—Velocity dispersion profile of 0047−281 along the major axis. The box height indicates the 68% measurement error, whereas the box width indicates the spectroscopic aperture (times the slit width, 1″.25). The squares show the corresponding values for an isotropic constant-M/L model, whereas the stars are for a model with 10% lower $M_{\rm E}$ (twice its error) and 10% higher R_e (both of which lower σ) with $r_i = \infty$. The circles indicate the isotropic Hernquist luminous component embedded in a total mass distribution with $\gamma' = 1.90$. See § 6 for details.

6.2. *Constant-M/L Models*

A stellar M/L of $M_*/L_B = (5.4 \pm 0.8)\, h_{65}\, M_\odot/L_{B,\odot}$ is required to account for the mass $M_{\rm E}$ enclosed by the Einstein radius. This is larger than the value $M_*/L_B = (3.1 \pm 1.0)\, h_{65}\, M_\odot/L_{B,\odot}$ derived from the FP evolution. If we had no kinematic information, this could only be interpreted as marginal evidence for dark matter inside the Einstein radius.

However, the velocity dispersion profile changes the situation dramatically: no model in which mass follows light can be found to fit the data. For example, in Figure 5 we show the velocity dispersion profile for an isotropic velocity distribution and constant-M/L model (*squares*). The dispersion falls too sharply with radius, and this model can be excluded at the greater than 99.9% CL. Even when R_e is increased by 10% and $M_{\rm E}$ decreased by 10% (twice its error)—both resulting in a smaller stellar velocity dispersion—the fit (*stars*) can still be excluded at the greater than 99.9% CL. Setting $r_i = R_e$ for the latter model (not shown) worsens the fit, and the model can be excluded at greater than 99.9% CL.

Strong, tangentially anisotropic models for lens galaxies (see, e.g., Romanowsky & Kochanek 1999), although probably not very likely, can lead to flatter velocity dispersion profiles, even if M/L is constant. We therefore tested models with constant negative values of β. For $\beta \lesssim -1.5$, we find that the dispersion profile indeed becomes flat.

However, the predicted stellar velocity dispersion is much higher (i.e., 240–260 km s^{-1}) than the observed values, and the model is excluded at greater than 99.9% CL. Models with $\beta \lesssim -1.5$ can only fit the data when M_E is lowered by $\sim$30%. This is at least 6 times the error on M_E and is incompatible with any acceptable lens model of 0047−281. We therefore conclude that mass does not follow light in the lens galaxy G of 0047−281, but that M/L must increase with radius. This is a key illustration that knowledge of the enclosed mass, M_E, inferred from the gravitational lens models, breaks the mass-anisotropy degeneracy.

6.3. *Stellar Mass and Dark Matter Slope*

We now turn to the two-component models described in § 5, to assess the density profile of the halo. In Figure 4, we show the likelihood contours (*dashed lines*) as a function of the stellar M/L (M_*/L_B) and inner slope of the dark matter halo (γ). We choose two representative values for the anisotropy radius, $r_i = R_e$ and $r_i = \infty$. Note that both the mass within the Einstein radius (M_E) and r_i are fixed for all models in Figures 4*a* and 4*b*. Hence, for each panel we effectively have two free parameters and three data points corresponding to the velocity dispersion profile (a fourth is given by the M_*/L_B measured by the evolution of the FP; § 3). We find that (1) for $M_*/L_B \rightarrow 0$, the slope of the dark matter halo γ approaches $\sim$2, consistent with the findings of § 6.1 (Fig. 4*c*); (2) for increasing values of M_*/L_B, the total density profile and the velocity dispersion profile become steeper. Hence, γ must decrease to fit the data.

When we include constraints on M_*/L_B from the FP (§ 3), the limits tighten on both M_*/L_B and γ (Fig. 4, *solid contours*). Remarkably, we find that the stellar M/L inferred from the FP agrees well with the maximum stellar M/L allowed by our isotropic dynamical models (as for MG 2016+112; TK02). Such a "maximum-bulge solution" is in that sense equivalent to the "maximum-disk solution" for spiral galaxies (see, e.g., van Albada & Sancisi 1986). We note, however, that the uncertainties are still considerable. In addition, the following limits are found: (1) $M_*/L_B = 3.2^{+0.2}_{-0.9}\ h_{65}\ M_\odot/L_{B,\odot}$ and $\gamma < 1.55$ (68% CL) for $r_i = \infty$ and (2) $M_*/L_B = 2.5^{+0.3}_{-0.5}\ h_{65}\ M_\odot/L_{B,\odot}$ and $\gamma < 1.12$ (68% CL) for $r_i = R_e$. Because the velocity dispersion profile steepens with increasing radial anisotropy, a smaller γ is required to retain a relatively flat dispersion profile. This explains the mild degeneracy between r_i and γ.

In the context of adiabatic contraction (AC) models (see, e.g., Blumenthal et al. 1986; Mo, Mao, & White 1998), the initial slope (γ_i) of the dark matter halo, i.e., before baryons assembled in the dark matter potential well, is in general expected to be shallower than the observed dark matter slope (γ). We find that the difference between γ_i and γ is relatively small, because the stellar mass in the case of 0047−280 is quite extended (i.e., large effective radius) and therefore affects the dark matter slope less than in MG 2016+112 (TK02), for example. Even in the absence of AC, however, we find that $\gamma_i = 1.5$ (Moore et al. 1998; Ghigna et al. 2000) is inconsistent with the results from 0047−281 at the 90% (68%) CL for $r_i = R_e(\infty)$, whereas the NFW profile ($\gamma_i = 1$; NFW) is consistent at the 68% CL for $r_i > R_e$. However, any mechanism, including AC, that steepens the initial slope by more than $\Delta\gamma = \gamma - \gamma_i \approx 0.6$ would imply that the results from 0047−281 are inconsistent with CDM simulations.

7. SUMMARY AND DISCUSSION

We have presented *HST* and Keck observations of the gravitational lens system 0047−281. In particular, *HST* images have been used to measure the surface photometry of the lens galaxy G and to build a simple lens model of the quadruple-image system. Keck-ESI data have been used to measure a spatially resolved velocity dispersion profile extended beyond the effective radius with exquisite accuracy ($\sim$5%). We have combined all these measurements to study the internal structure and dynamics of the lens galaxy at $z = 0.485$, finding the following:

1. The offset of galaxy G from the local FP, $\Delta \log(M/L_B) = -0.37 \pm 0.06$ between $z = 0$ and 0.485, is consistent with what is observed for field E/S0 galaxies at similar redshift (T02), i.e., somewhat larger than for cluster E/S0 galaxies. In terms of pure luminosity evolution, this could be explained with intermediate-age single stellar populations, or, more likely, with secondary episodes of star formation contributing a fraction of young stars to an old underlying stellar population (see discussion in T02).

2. Models with no dark matter and constant-M/L models are excluded at greater than 99.9% CL. Also, constant-M/L models with strongly tangential anisotropy of the stellar velocity ellipsoid are excluded at greater than 99.9% CL.

3. The stellar M/L $M_*/L_B = (3.1 \pm 1.0)\ h_{65}\ M_\odot/L_{B,\odot}$ obtained from the offset of the FP is inconsistent with the value required to fully account for M_E, $M_*/L_B = 5.4\ h_{65}\ M_\odot/L_{B,\odot}$. This suggests the presence of dark matter. The FP value is consistent with what is obtained with our two-component dynamical models, and combining the two constraints, we find $M_*/L_B = 3.2^{+0.2}_{-0.9}\ h_{65}\ M_\odot/L_{B,\odot}$ (68% CL) for an isotropic velocity ellipsoid. Hence, dark matter comprises a fraction of $0.41^{+0.05}_{-0.15}$ of the total mass enclosed by the Einstein radius of $8.70\ h_{65}^{-1}$ kpc for $r_i = \infty$. For $r_i = R_e$, this fraction increases to $0.54^{+0.09}_{-0.06}$. The data are also consistent with an Osipkov-Merritt radial anisotropy with anisotropy radius $r_i \geq 0.7 R_e$ (68% CL).

4. The total (luminous plus dark) mass distribution inside the Einstein radius can be described by a single power-law density distribution, $\rho_t \propto r^{-\gamma'}$, with $\gamma' = 1.90 \pm 0.05$ (68% CL) for isotropic models, i.e., $r_i = \infty$. In general, $\gamma' = 1.90^{+0.05}_{-0.23}$ (68% CL) is found. The systematic error is estimated at 0.1.

5. An upper limit, $\gamma \lesssim 1.55$ (68% CL), is found on the slope on the dark matter halo inside the Einstein radius for an isotropic model. This limit tightens to $\gamma \lesssim 1.12$ for mildly anisotropic models with $r_i = R_e$. Initial dark matter profiles with $\gamma_i = 1.5$ (Moore et al. 1998; Ghigna et al. 2000) are therefore only marginally acceptable, especially since the profile is expected to be less steep before the galaxy assembled. If γ steepens by $\Delta\gamma > 0.6$ during galaxy formation, all CDM simulations are inconsistent with our results.

In summary, the lens galaxy in 0047−281 appears to convey the same picture formulated for MG 2016+112, that early-type galaxies at significant look-back times can be effectively described by an $R^{1/4}$ luminous component (modeled in this paper as either a Hernquist or Jaffe profile) embedded in a nearly isothermal total mass distribution and that their stellar velocity dispersion is relatively isotropic, in particular inside the effective radius. In fact, lens galaxies in both MG 2016+112 (KT02; TK02) and 0047−281 show that the total mass distribution is well approximated to

within 5% by a simple power-law density profile, $\rho_t \propto r^{-2}$ (i.e., isothermal). Whether this conclusion can be generalized, however, requires the analysis of more systems.

Furthermore, we have shown that deviations from isothermality or isotropy in the lens galaxies of 0047−281 and MG 2016+112 quickly lead to inconsistencies with constraints from the FP, the observed stellar kinematics, the stellar M/L, observations of local E/S0 galaxies, or the gravitational lens models, whereas the models that fit all constraints are internally consistent, appear to agree with all observational constraints available, and indicate both isothermality and near-isotropy. Constant-M/L or steep mass profiles inside the Einstein radius are excluded at very high confidence levels.

A physical explanation is required *if* isotropy and the almost perfect isothermality are confirmed to be generic features of early-type galaxies. In particular, this regularity might suggest that luminous and dark matter were strongly coupled at some point during galaxy assembly. Whereas AC has been suggested as a mechanism that can lead to near-isothermal mass profiles (see, e.g., Keeton 2001), it is not clear why such a process should *only* stop when the density profile is isothermal to better than apparently a few percent (see also TK02). AC also leads to a slope of the inner density profile, inconsistent with the observed absence of lensed images in the centers of lens galaxies (see, e.g., Keeton 2001), if either the central black holes are not very massive or the inner density profiles do not steepen through some other process. Violent relaxation could be a natural and viable explanation for this regularity, although it should also be explained why luminous and dark matter have *different* density profiles (see discussion in TK02 and references therein). A combination of the two processes during some period in the formation of the galaxy cannot be excluded.

The striking similarity of the internal structure of E/S0 galaxies at large look-back times to that of local E/S0 galaxies (see, e.g., Franx, van Gorkom, & de Zeeuw 1994; Bertin et al. 1994; Rix et al. 1997; Gerhard et al. 2001; see also Kochanek 1995 and reviews by de Zeeuw & Franx 1991; Bertin & Stiavelli 1993; Merritt 1999) suggests that little structural evolution occurred during the past 8 Gyr (although, again, a larger sample is needed to make a quantitative and general statement). The lack of significant structural evolution is also suggested by the remarkable agreement between the stellar M_*/L_B obtained with our dynamical models and the stellar M_*/L_B estimated using the FP evolution. This fact adds further evidence in favor of a scenario in which the general population of massive (field) E/S0 galaxies changed little in the past 8 Gyr (from $z \sim 1$)—as indicated, for example, by the modest evolution in their number density (Schade et al. 1999; Im et al. 2002; Cohen 2002; McCarthy et al. 2001) and by the little evolution in the scatter of the FP (T02)—with most of the evolution being driven by aging of old stars and secondary episodes of star formation (Jimenez et al. 1999; Trager et al. 2000; Menanteau, Abraham, & Ellis 2001; T02).

We thank Eric Agol, Andrew Benson, Giuseppe Bertin, Roger Blandford, Richard Ellis, Chris Kochanek, and Massimo Stiavelli for useful comments on this manuscript and stimulating conversations. We thank the referee for the comments that helped clarify the presentation of our results. The use of the Gauss-Hermite Pixel-Fitting Software and Gauss-Hermite Fourier-Fitting Software developed by R. P. van der Marel and M. Franx is gratefully acknowledged. The ESI data were reduced using software developed in collaboration with D. Sand. We acknowledge the use of the *HST* data collected by the CASTLES collaboration. L. V. E. K. and T. T. acknowledge support by grants from NSF and NASA (AST 99-00866; STScI-GO 06543.03-95A; STScI-AR-09222). We thank J. Miller, M. Bolte, R. Guhathakurta, D. Zaritsky, and all the people who worked to make ESI such a nice instrument. Finally, the authors wish to recognize and acknowledge the very significant cultural role and reverence that the summit of Mauna Kea has always had within the indigenous Hawaiian community. We are most fortunate to have the opportunity to conduct observations from this mountain.

REFERENCES

Bender, R., Saglia, R. P., Ziegler, B., Belloni, P., Greggio, L., Hopp, U., & Bruzual, G. 1998, ApJ, 493, 529
Bertin, G., Ciotti, L., & del Principe, M. 2002, A&A, 386, 149
Bertin, G., & Stiavelli, M. 1993, Rep. Prog. Phys., 56, 493
Bertin, G., et al. 1994, A&A, 292, 381
Binney, J., & Tremaine, S. 1987, Galactic Dynamics (Princeton: Princeton Univ. Press)
Blumenthal, G. R., Faber, S. M., Flores, R., & Primack, J. R. 1986, ApJ, 301, 27
Bullock, J. S., Kolatt, T. S., Sigad, Y., Somerville, R. S., Kravtsov, A. V., Klypin, A. A., Primack, J. R., & Dekel, A. 2001, MNRAS, 321, 559
Chen, G. H., Kochanek, C. S., & Hewitt, J. N. 1995, ApJ, 447, 62
Ciotti, L. 1999, ApJ, 520, 574
Ciotti, L., Lanzoni, B., & Renzini, A. 1996, MNRAS, 282, 1
Cohen, J. G. 2002, ApJ, 567, 672
Cohn, J. D., Kochanek, C. S., McLeod, B. A., & Keeton, C. R. 2001, ApJ, 554, 1216
de Zeeuw, T., & Franx, M. 1991, ARA&A, 29, 239
Djorgovski, S. G., & Davis, M. 1987, ApJ, 313, 59
Dressler, A., Lynden-Bell, D., Burstein, D., Davies, R. L., Faber, S. M., Terlevich, R., & Wegner, G. 1987, ApJ, 313, 42
Franx, M., van Gorkom, J. H., & de Zeeuw, T. 1994, ApJ, 436, 642
Fruchter, A. S., & Hook, R. N. 2002, PASP, 114, 144
Gerhard, O., Kronawitter, A., Saglia, R. P., & Bender, R. 2001, AJ, 121, 1936
Ghigna, S., Moore, B., Governato, F., Lake, G., Quinn, T., & Stadel, J. 2000, ApJ, 544, 616
Grogin, N. A., & Narayan, R. 1996, ApJ, 464, 92
Hernquist, L. 1990, ApJ, 356, 359
Im, M., et al. 2002, ApJ, 571, 136
Jaffe, W. 1983, MNRAS, 202, 995
Jimenez, R., Friaça, A. C. S., Dunlop, J. S., Terlevich, R. J., Peacock, J. A., & Nolan, L. A. 1999, MNRAS, 305, L16
Jørgensen, I., Franx, M., Hjorth, J., & van Dokkum, P. G. 1999, MNRAS, 308, 833
Keeton, C. R. 2001, ApJ, 561, 46
Kelson, D. D., Illingworth, G. D., van Dokkum, P. G., & Franx, M. 2000, ApJ, 531, 137
Kelson, D. D., van Dokkum, P. G., Franx, M., Illingworth, G. D., & Fabricant, D. 1997, ApJ, 478, L13
Kochanek, C. S. 1991, ApJ, 371, 289
———. 1994, ApJ, 436, 56
———. 1995, ApJ, 445, 559
Kochanek, C. S., et al. 2000, ApJ, 543, 131
Koopmans, L. V. E., & Fassnacht, C. D. 1999, ApJ, 527, 513
Koopmans, L. V. E., Garrett, M. A., Blandford, R. D., Lawrence, C. R., Patnaik, A. R., & Porcas, R. W. 2002, MNRAS, 334, 39
Koopmans, L. V. E., & Treu, T. 2002, ApJ, 568, L5 (KT02)
Kormann, R., Schneider, P., & Bartelmann, M. 1994, A&A, 284, 285
Kronawitter, A., Saglia, R. P., Gerhard, O., & Bender, R. 2000, A&AS, 144, 53
McCarthy, P. J., et al. 2001, ApJ, 560, L131
Menanteau, F., Abraham, R. G., & Ellis, R. S. 2001, MNRAS, 322, 1
Merritt, D. 1985a, AJ, 90, 1027
———. 1985b, MNRAS, 214, 25P
———. 1999, PASP, 111, 129
Merritt, D., & Aguilar, L. A. 1985, MNRAS, 217, 787
Mo, H. J., Mao, S., & White, S. D. M. 1998, MNRAS, 295, 319
Moore, B., Governato, F., Quinn, T., Stadel, J., & Lake, G. 1998, ApJ, 499, L5

Muñoz, J. A., Kochanek, C. S., & Keeton, C. R. 2001, ApJ, 558, 657
Navarro, J., Frenk, C. S., & White, S. D. M. 1997, ApJ, 490, 493 (NFW)
Osipkov, L. P. 1979, AZh Pis'ma, 5, 77
Pahre, M. A. 1998, Ph.D. thesis, California Institute of Technology
Rix, H.-W., de Zeeuw, P. T., Cretton, N., van der Marel, R. P., & Carollo, C. M. 1997, ApJ, 488, 702
Romanowsky, A. J., & Kochanek, C. S. 1999, ApJ, 516, 18
Rusin, D., Norbury, M., Biggs, A. D., Marlow, D. R., Jackson, N. J., Browne, I. W. A., Wilkinson, P. N., & Myers, S. T. 2002, MNRAS, 330, 205
Rusin, D., & Tegmark, M. 2001, ApJ, 553, 709
Saglia, R. P., Bertin, G., & Stiavelli, M. 1992, ApJ, 384, 433
Saha, P. 2000, AJ, 120, 1654
Schade, D., et al. 1999, ApJ, 525, 31
Schlegel, D. J., Finkbeiner, D. P., & Davis M. 1998, ApJ, 500, 525
Sheinis, A. I., Bolte, M., Epps, H. W., Kibrick, R. I., Miller, J. S., Radovan, M. V., Bigelow, B.C., & Sutin, B. M. 2002, PASP, 114, 851
Stiavelli, M., & Sparke, L. S. 1991, ApJ, 382, 466
Surpi, G., & Blandford, R. D. 2003, ApJ, in press
Trager, S. C., Faber, S. M., Worthey, G., & González, J. J. 2000, AJ, 119, 1645
Treu, T., & Koopmans, L. V. E. 2002, ApJ, 575, 87 (TK02)
Treu, T., Stiavelli, M., Bertin, G., Casertano, C., & Møller, P. 2001a, MNRAS, 326, 237 (T01a)
Treu, T., Stiavelli, M., Casertano, C., Møller, P., & Bertin, G. 1999, MNRAS, 308, 1037 (T99)
———. 2002, ApJ, 564, L13 (T02)
Treu, T., Stiavelli, M., Møller, P., Casertano, C., & Bertin, G. 2001b, MNRAS, 326, 221 (T01b)
van Albada, T. S. 1982, MNRAS, 201, 939
van Albada, T. S., & Sancisi, R. 1986, Philos. Trans. R. Soc. London, A, 320, 447
van der Marel, R. P. 1994, MNRAS, 270, 271
van der Marel, R. P., & Franx, M. 1993, ApJ, 407, 525
van Dokkum, P. G., & Franx, M. 1996, MNRAS, 281, 985
van Dokkum, P. G., Franx, M., Kelson, D. D., & Illingworth, G. D. 1998, ApJ, 504, L17
———. 2001, ApJ, 553, L39
Warren, S. J., Hewett, P. C., Lewis, G. F., Møller, P., Iovino, A., & Shaver, P. A. 1996, MNRAS, 278, 139
Warren, S. J., Iovino, A., Hewett, P. C., & Shaver, P. A. 1998, MNRAS, 299, 1215
Warren, S. J., Lewis, G. F., Hewett, P. C., Møller, P., Shaver, P. A., & Iovino, A. 1999, A&A, 343, L35
Wucknitz, O. 2002, MNRAS, 332, 951
Ziegler, B. L., Bower, R. G., Smail, I., Davies, R. L., & Lee, D. 2001, MNRAS, 325, 1571